

# High order interpolation of magnetic fields with vector potential reconstruction for particle simulations

O. Beznosov,<sup>1</sup> J. Bonilla,<sup>1</sup> G. A. Wimmer,<sup>1</sup> and X.-Z. Tang<sup>1</sup>  
 Los Alamos National Laboratory

(\*Electronic mail: obeznosov@lanl.gov.)

(Dated: Monday 6<sup>th</sup> January, 2025)

We propose a method for interpolating divergence-free continuous magnetic fields via vector potential reconstruction using Hermite interpolation, which ensures high-order continuity for applications requiring adaptive, high-order ordinary differential equation (ODE) integrators, such as the Dormand-Prince method. The method provides  $C(m)$  continuity and achieves high-order accuracy, making it particularly suited for particle trajectory integration and Poincaré section analysis under optimal integration order and timestep adjustments. Through numerical experiments, we demonstrate that the Hermite interpolation method preserves volume and continuity, which are critical for conserving toroidal canonical momentum and magnetic moment in guiding center simulations, especially over long-term trajectory integration. Furthermore, we analyze the impact of insufficient derivative continuity on Runge-Kutta schemes and show how it degrades accuracy at low error tolerances, introducing discontinuity-induced truncation errors. Finally, we demonstrate performant Poincaré section analysis in two relevant settings of field data collocated from finite element meshes.

## I. INTRODUCTION

Electromagnetics and plasma simulations are subject to a fundamental physics constraint on the magnetic field  $\mathbf{B}$ , which is zero divergence ( $\nabla \cdot \mathbf{B} = 0$ ) or the absence of magnetic monopoles. There are two common approaches to address this physics constraint in discrete mathematics. One less deliberate approach is to control the non-vanishing  $\nabla \cdot \mathbf{B}$  below the level of discretization error, by introducing a so-called divergence cleaning term in the equation.<sup>1-3</sup>

More elaborate approaches aim to enforce  $\nabla \cdot \mathbf{B} = 0$  in the design of numerical discretizations. A representative method is the mimetic finite difference method,<sup>4-10</sup> in which the magnetic field is discretized as a surface normal on each cell surface, shared by neighboring cells on both sides of the cell surface. The discrete numerical divergence, evaluated at the cell center, strictly remains divergence-free if the initial field satisfies  $\nabla \cdot \mathbf{B} = 0$ . The Yee mesh in particle-in-cell simulation<sup>11</sup> is an early realization of this approach and has found applications in a wide range of plasma physics problems.

For integrating magnetic field line characteristics, which is required in diagnosing magnetic topology and/or evolving parallel transport, and for tracing charged particle characteristics, especially that of the guiding center, one would desire  $\nabla \cdot \mathbf{B} = 0$  everywhere in the simulation domain. Standard interpolation schemes of a discrete mimetic  $\mathbf{B}$  field cannot provide this property, even though they are commonly used in Poincaré section analysis and particle orbit tracing. The situation is further aggravated if  $\nabla \cdot \mathbf{B}$  is not even satisfied discretely in the numerical discretization, in which case one often finds Poincaré section analysis impossible to perform or that the results are simply nonsensical. Finn and Chacon<sup>12</sup> proposed an approach that enforces  $\nabla \cdot \mathbf{B} = 0$  through reconstruction. The idea is to first construct the vector potential  $\mathbf{A}_D$  on discrete grid points from the numerical/discrete  $\mathbf{B}_D$ , and then spline fit the discrete  $\mathbf{A}_D$  for a globally smooth vector potential  $\mathbf{A}$ . The final step involves taking the analytical derivative of the vector potential components for  $\mathbf{B} = \nabla \times \mathbf{A}$ , which is divergence-free everywhere in the simulation domain. This approach has proven to produce sensible Poincaré section plots; namely, nested flux surfaces remain sharp, and separatrix crossing can be clearly identified in the transition to field line chaos. In other words, the reconstruction scheme can reliably project a discrete vector field, even if it is not divergence-free, onto the space of divergence-free vectors.

The purpose of this paper is to quantify the accuracy of such a reconstruction scheme. This appears to be a meaningful problem only if the discrete  $\mathbf{B}_D$  field is mimetic in the first place. In addition to Poincaré section analysis, we are particularly interested in how such a reconstructed magnetic field impacts the accuracy of the guiding center integration. This is motivated by the application of Lagrangian and semi-Lagrangian integration of the relativistic drift-kinetic equation, which has found critical importance in understanding the runaway electron dynamics in a tokamak disruption.<sup>13,14</sup>

There are a number of factors that determine the accuracy of the reconstruction scheme. The first concerns the numerical integration that constructs the vector potential from the magnetic field data on a computational grid. The second is the interpolation scheme for the discrete vector potential data that produces the globally smooth  $\mathbf{A}$ , from which  $\mathbf{B} = \nabla \times \mathbf{A}$  can be evaluated everywhere in the simulation domain. The third is the numerical integration of the guiding center trajectory using the interpolated field data.

In place of the cubic spline, we are interested in how Hermite interpolation can provide a useful alternative. This was partly motivated by the recent success in applying Hermite interpolation to construct highly accurate and stable solvers of partial differential equations (PDEs)<sup>15-17</sup>, and by the relative ease in computing the high-order Hermite interpolants,

compared with the cubic spline. We were also attracted to Hermite interpolation for its attribute of not overfitting. The basics of Hermite interpolation are explained in section III.

What we have learned is that achieving accuracy and smoothness of the interpolated magnetic field requires care in the very first step of reconstructing the vector potential  $\mathbf{A}$  from the discrete  $\mathbf{B}_D$  data on the grid. This concerns the spatial integration of the magnetic field for the vector potential components, as discussed in section IV. For accuracy, we find that analytical integration of Hermite interpolation of the  $\mathbf{B}$  data is a superior approach compared with the usual line integration by numerical quadratures. Since Hermite interpolation, by matching the derivatives up to the  $m$ th order with the data, can achieve an order of  $2m + 1$  in the interpolating polynomials, we anticipate globally smooth fitting of the vector potential, as long as the numerical derivatives of the discrete field data on the grid points are reasonably well-behaved.

The smoothness in the reconstructed  $\mathbf{A}$  and the resulting divergence-free magnetic field  $\mathbf{B}$  is conducive to higher-order integration of the guiding center trajectories. This is because high-order ordinary differential equation (ODE) integration schemes, such as Runge-Kutta (RK), are based on Taylor expansion. Thus, their accuracy depends on the existence of smooth high-order derivatives. Since the smoothness of the trajectories follows from the smoothness of the governing field<sup>18</sup>, for coherent and consistent reconstruction of particle trajectories, the high-order smoothness of the background fields becomes paramount.

Our numerical experiments indicate that, indeed, whether the RK method can optimally converge for Poincaré section analysis and particle trajectory integration depends on the smoothness of the reconstructed magnetic field. As theoretically shown<sup>19</sup>, the order conditions must be satisfied for the RK method, say of the 5th order as in the Dormand-Prince 4(5) pair, to properly adjust the timestep. This requires derivatives up to the fourth order to cancel in certain linear combinations of RK stages, defined by a Butcher tableau.

The rest of the paper is organized as follows. In section II, we demonstrate the reduction in the order of accuracy of Runge-Kutta methods on a simple problem to further motivate the use of Hermite interpolation and show what we expect to see in our numerical experiments with magnetic fields. Section III introduces the Hermite interpolation method. The construction of a vector potential from the discrete magnetic field data is presented in section IV. Various numerical experiments, including the use of magnetic field data from both finite element and mimetic finite difference MHD codes, are reported in section V. Section VI concludes the paper with a summary.

## II. CONVERGENCE ORDER REDUCTION IN HIGH ORDER ODE SOLVERS

As conventionally defined<sup>19</sup>, an RK method with time step  $\Delta t$  has order  $p$  if, for sufficiently smooth problems, the Taylor series for the exact solution  $y(t_0 + \Delta t)$  and numerical solution  $y_1$  agree with each other up to the term  $\Delta t^p$ . In practice, Runge-Kutta type methods are also frequently used to solve ODEs whose right-hand sides do not provide such smoothness or in some cases are even discontinuous. This may for instance occur for ODEs resulting from PDEs that are discretized in space using non-smooth finite element or finite difference methods. Correspondingly, the lack of a Taylor series may then deteriorate the expected convergence rate, which we will demonstrate with a simple example of a non-autonomous ODE. However, smoothness can be restored by means of Hermite interpolation, which is particularly useful where high-order ODE integration is desirable.

Consider a first order ODE,

$$y' = f(t), \quad y(0) = 0, \quad (1)$$

with a piecewise right-hand side

$$f(t) = \begin{cases} f_1(t), & t \leq \frac{1}{2}, \\ f_2(t), & t > \frac{1}{2}. \end{cases} \quad (2)$$

The exact solution at the end point  $t = 1$  can be written as an integral over the full time interval,

$$y(1) = \int_0^1 f(t) dt. \quad (3)$$

To further study the aforementioned effect of non-smoothness, we set up a numerical experiment choosing  $f_1$  and  $f_2$  such that  $f_1(\frac{1}{2}) = f_2(\frac{1}{2})$ ,  $f_1'(\frac{1}{2}) = f_2'(\frac{1}{2})$  and  $f_1''(\frac{1}{2}) - f_2''(\frac{1}{2}) = \epsilon$ . Numerically integrating (1) with a fixed time step using the embedded Dormand-Prince Runge-Kutta pair<sup>20</sup>, we obtain convergence plots as given in FIG. 1, depicting both the method's 5<sup>th</sup> and embedded 4<sup>th</sup> order solutions for a range of values for  $\epsilon$ . For an even total number of time steps, both solutions converge at the expected rate, while for an odd number the solutions' convergence order deteriorates from 5 to 3 and from 4 to 3.5 for the two solutions, respectively. The decreased convergence rate for an odd number of time steps is in line with our above discussion on smoothness. On the other hand, the optimal convergence for an even number of time

steps follows since in this case one of the discrete points in time is exactly at the 2nd derivative discontinuity at  $t = \frac{1}{2}$ , and therefore locally, the right-hand side function fed into the RK algorithm is always perfectly smooth. Finally, the negative effect for an odd number of time steps decreases as  $\varepsilon$  is decreased, that is as the discontinuous gap at  $t = \frac{1}{2}$  narrows. In particular, small values of  $\varepsilon$  – corresponding to a “almost regular” right-hand side – lead to convergence rates that may still be deemed acceptable in practice.

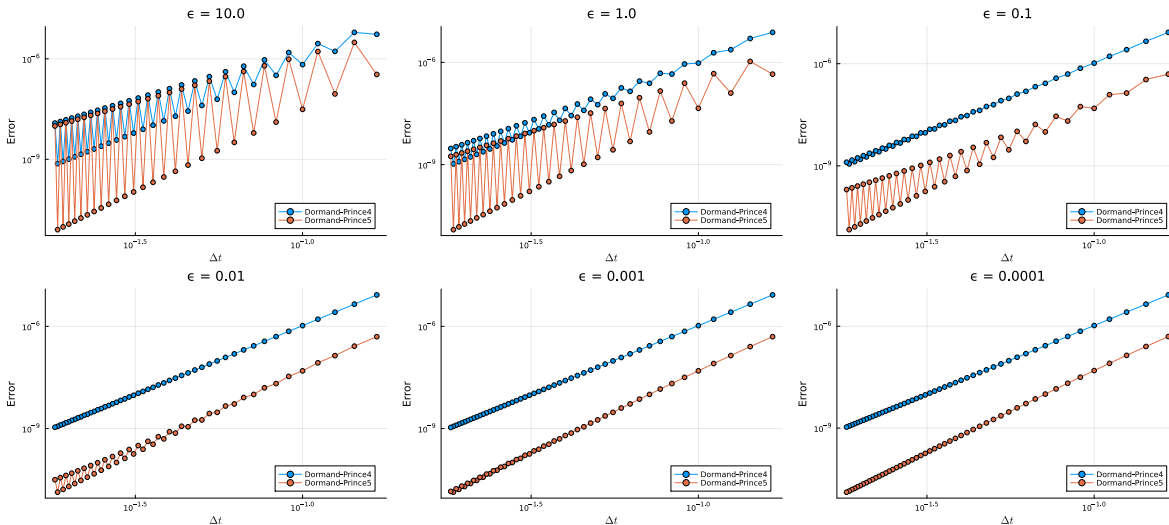


FIG. 1: Convergence rates for 4th order (blue curves) and 5th order (red curves) solutions to the Dormand-Prince Runge-Kutta method. Curves display numerical error from integrating (1) for a right-hand side with second derivative discontinuity of varying magnitude  $\varepsilon \in [10^{-4}, 10]$ . The error is shown as a function of time step size, and oscillations arise from passing through time step sizes that alternatingly lead an even and odd number of total time steps.

Similar cases can be constructed for autonomous systems, but for the general case  $y' = f(y)$ , standard time stepping methods are unlikely to always step exactly on given discontinuities. Importantly, as seen in the above example for the Dormand-Prince method, adaptive timestepping capabilities may deteriorate due to the reduced convergence rates in the presence of non-smoothness, forcing the method to march at a minimal timestep<sup>19</sup>. To avoid this, one could employ dense output – using e.g. Hermite interpolation – and trajectory inversion techniques in order to not step over discontinuities. Alternatively, one could impose high-order continuity to begin with by applying a high-order Hermite interpolation method on the ODE’s right-hand side, and this is the approach covered in this work.

### III. HERMITE INTERPOLATION

We briefly present the Hermite interpolation method here and refer the reader to the original work on Hermite methods for wave equations<sup>16</sup> for error analysis and other details. For ease of exposition, we first demonstrate a one-dimensional approximation and then show how to extend it to higher dimensions.

Let the spatial domain be  $D = [a, b]$ , discretized by a primal grid

$$\Omega_p = \{x_i : x_i = a + ih, i = 0, \dots, N\}, \quad (4)$$

with corresponding dual grid

$$\Omega_d = \left\{x_j : x_j = a + jh, j = \frac{1}{2}, \dots, N - \frac{1}{2}\right\}. \quad (5)$$

At the primal grid  $\Omega_p$ , we store the target function  $f$  and its  $m$  derivatives, represented by Taylor polynomials of order  $m$ . At the dual grid  $\Omega_d$ , we center local polynomials that match the target function and its  $m$  derivatives at primal grid points. First, we obtain the polynomials as approximations to the target function on the primal grid

$$f(x) \approx \sum_{l=0}^m \hat{u}_l \left(\frac{x - x_i}{h}\right)^l, \quad x_i \in \Omega_p. \quad (6)$$

The coefficients  $\hat{u}_l$  are assumed to be accurate approximations to the scaled Taylor coefficients of the target function. If expressions for the derivatives were known, for example from an underlying high order method, we could simply set

$$\hat{u}_l = \frac{h^l}{l!} \frac{d^l f}{dx^l}(x_i), \quad x_i \in \Omega_p. \quad (7)$$

If the derivatives are not available, we can instead use finite difference approximations on a finer grid. In our numerical experiments, these coefficients are evaluated with centered finite differences<sup>21</sup> as follows

$$\hat{u}_0 = f(x_i), \quad (8)$$

$$\hat{u}_1 = h \cdot \frac{-f(x_i + 2\Delta x) + 8f(x_i + \Delta x) - 8f(x_i - \Delta x) + f(x_i - 2\Delta x)}{12\Delta x}, \quad (9)$$

$$\hat{u}_2 = \frac{h^2}{2} \cdot \frac{-f(x_i + 2\Delta x) + 16f(x_i + \Delta x) - 30f(x_i) + 16f(x_i - \Delta x) - f(x_i - 2\Delta x)}{12\Delta x^2}, \quad (10)$$

where the fine grid length scale  $\Delta x$  would be a fraction of  $h$ . To compute derivatives at boundaries left/right stencils<sup>21</sup> can be exploited. This suggests primal and dual grids used in Hermite interpolation can be coarser than the original grid, where data is available, without loss of information. In contrast, this would not be the case with tricubic spline interpolation. Note that the expressions (8)-(10) are fourth order finite difference approximations for the first and the second derivatives. Alternatively, projection<sup>17</sup> or interpolation methods could be used to find the coefficients in (6).

### A. Hermite interpolation in 1D

Next, we consider an interval bounded by two neighboring grid points  $x_i, x_{i+1} \in \Omega_p$  and construct the unique local Hermite interpolating polynomial of degree  $(2m+1)$ , centered on the dual grid point  $x_j \in \Omega_d, j = i + \frac{1}{2}$ . The interpolating polynomials can be written in Taylor form

$$u_j(x) = \sum_{l=0}^{2m+1} \hat{u}_{j,l} \left( \frac{x-x_j}{h} \right)^l, \quad j = \frac{1}{2}, \dots, N - \frac{1}{2}. \quad (11)$$

The interpolating polynomial  $u_{i+\frac{1}{2}}$  is determined by the local interpolation conditions

$$\left( \frac{d^l u_j}{dx^l} = \frac{d^l u_i}{dx^l} \right) \Big|_{x=x_i}, \quad \left( \frac{d^l u_j}{dx^l} = \frac{d^l u_{i+1}}{dx^l} \right) \Big|_{x=x_{i+1}}, \quad l = 0, \dots, m, \quad j = i + \frac{1}{2}, \quad (12)$$

and we find the coefficients in (11) by forming a generalized Newton table as described in<sup>22</sup>.

### B. Differentiation and integration

The piece-wise Hermite interpolation polynomials have a local monomial basis and thus are easy to differentiate and integrate analytically by shifting and rescaling the coefficients. The resulting derivatives can be expressed in Taylor form as well. The derivative of the polynomial (11) is

$$\frac{d^n}{dx^n} u_j(x) = \sum_{l=0}^{2m+1-n} \frac{(l+1) \dots (l+n)}{h^n} \hat{u}_{j,l+n} \left( \frac{x-x_j}{h} \right)^l. \quad (13)$$

Further, its indefinite integral is

$$\int u_j(x) dx = \sum_{l=1}^{2m+2} \frac{h}{l} \hat{u}_{j,l-1} \left( \frac{x-x_j}{h} \right)^l. \quad (14)$$

and integrating over dual cell endpoints, we obtain

$$\int_{x_j - \frac{h}{2}}^{x_j + \frac{h}{2}} u_j(x) dx = \sum_{k=0}^m \frac{h}{2k+1} \hat{u}_{j,2k} \left( \frac{1}{2} \right)^{2k}. \quad (15)$$

Note that the expressions (13)-(15) are exact. By combining (14) and (15), we can compute the approximation to the integral of  $u$  from an arbitrary dual grid point  $x_j$  to an arbitrary point  $y \in [x_k - \frac{h}{2}, x_k + \frac{h}{2}]$  with  $j < k$  as

$$\begin{aligned}
\int_{x_j}^x f(x') dx' &\approx \int_{x_j}^{x_j+\frac{h}{2}} u_j(x) dx + \sum_{j'=j+1}^{k-1} \int_{x_{j'}-\frac{h}{2}}^{x_{j'}+\frac{h}{2}} u_{j'}(x) dx + \int_{x_k-\frac{h}{2}}^x u_j(x) dx \\
&= \sum_{l=1}^{2m+2} \frac{h}{l} \left[ \sum_{j'=j}^{k-1} \hat{u}_{j',l-1} \left( \frac{1}{2} \right)^l - \sum_{j'=j+1}^k \hat{u}_{j',l-1} \left( -\frac{1}{2} \right)^l \right] + \sum_{l=1}^{2m+2} \frac{h}{l} \hat{u}_{k,l-1} \left( \frac{x-x_k}{h} \right)^l. \tag{16}
\end{aligned}$$

This defines an approximation to the anti-derivative of  $u$  written in Taylor form.

### C. Higher dimensions

In higher dimensions the approximations to  $u$  take the form of centered tensor product Taylor polynomials. In the case of cylindrical coordinates – which are often considered in tokamak fusion reactor descriptions – the coefficients would be of the form  $\hat{u}_{l,s;k}^{j_1,j_2}$ , with superscripts representing cell indices of the  $(R,Z)$  poloidal plane. Further, the first two subscripts represent powers in the two spatial directions of the poloidal plane, and the third represents the angular (toroidal) coordinate  $\varphi$ . Since the  $\varphi$ -direction is periodic, a smooth, easy to differentiate approximation can be achieved by using trigonometric polynomials. In particular, a single, constant coefficient in the  $\varphi$  direction would correspond to axisymmetric fields.

Altogether, we consider tensor product Taylor-trigonometric polynomials given by

$$u^{i_1,i_2}(R, \varphi, Z) = \sum_{k=0}^{N_\varphi} \sum_{l=0}^{m_R} \sum_{s=0}^{m_Z} \hat{u}_{l,s;k}^{i_1,i_2} \left( \frac{R-R_{i_1}}{h_R} \right)^l \left( \frac{Z-Z_{i_2}}{h_Z} \right)^s T_k(\varphi), \quad i_1 = 0, \dots, N_R, \quad i_2 = 0, \dots, N_Z, \tag{17}$$

where  $T_k$  is a desired trigonometric polynomial basis. In this work we use a real discrete Fourier transform of the field data in  $\varphi$ , with an associated basis

$$T_k(\varphi) = \begin{cases} \cos(k\varphi), & k = 0, \dots, \frac{N_\varphi}{2}, \\ \sin\left(\left(k - \frac{N_\varphi}{2}\right)\varphi\right), & k = \frac{N_\varphi}{2} + 1, \dots, N_\varphi. \end{cases} \tag{18}$$

A tensor product version of the finite differences (8)-(10) can be used to determine the poloidal coefficients. Further, we compute toroidal coefficients working out the finite differences in several equidistant poloidal planes and performing a Fourier transform for each index set  $(i_1, i_2, l, s)$ .

To perform Hermite interpolation in the two-dimensional poloidal plane, we apply sequences of one-dimensional Hermite interpolations as described in Section (III A) in two directions as follows. First, we form the polynomials  $p_{j_1,i_2}(R, Z)$  centered at each cell edge by performing  $(m_Z + 1)$   $R$ -interpolations, satisfying local interpolation conditions (12) for  $R$ , so that

$$\left[ \frac{d^n}{dR^n} \sum_{l=0}^{2m_R+1} \hat{u}_{l,s;k}^{j_1,i_2} \left( \frac{R-R_{j_1}^d}{h_R} \right)^l \right] \Big|_{R=R_{i_1}^p} = \left[ \frac{d^n}{dR^n} \sum_{l=0}^{m_R} \hat{u}_{l,s;k}^{i_1,i_2} \left( \frac{R-R_{i_1}^p}{h_R} \right)^l \right] \Big|_{R=R_{i_1}^p}, \tag{19}$$

$$\left[ \frac{d^n}{dR^n} \sum_{l=0}^{2m_R+1} \hat{u}_{l,s;k}^{j_1,i_2} \left( \frac{R-R_{j_1}^d}{h_R} \right)^l \right] \Big|_{R=R_{i_1+1}^p} = \left[ \frac{d^n}{dR^n} \sum_{l=0}^{m_R} \hat{u}_{l,s;k}^{i_1+1,i_2} \left( \frac{R-R_{i_1+1}^p}{h_R} \right)^l \right] \Big|_{R=R_{i_1+1}^p}, \quad j_1 = i_1 + \frac{1}{2}. \tag{20}$$

This results in  $(2m_R + 1) \times (m_Z + 1)$ -degree polynomials centered on intermediate grid points  $(R_{j_1}, Z_{i_2})$  located on vertical cell edges. Superscripts  $d$  and  $p$  indicate dual and primal grid points, respectively.

We then form polynomials  $p_{j_1,j_2}(R, Z)$  centered on dual grid points in cell centers by performing an additional  $(2m_R + 2)$   $Z$ -interpolations per dual grid point satisfying (19), (20). The above operations can be performed for each  $\varphi$ -mode independently and in parallel, and the resulting piece-wise polynomial becomes

$$u^{j_1,j_2}(R, \varphi, Z) = \sum_{k=0}^{N_\varphi} \sum_{l=0}^{2m_R+1} \sum_{s=0}^{2m_Z+1} \hat{u}_{l,s;k}^{j_1,j_2} \left( \frac{R-R_{j_1}^d}{h_R} \right)^l \left( \frac{Z-Z_{j_2}^d}{h_Z} \right)^s T_k(\varphi), \quad j_1 = \frac{1}{2}, \dots, N_R - \frac{1}{2}, \quad j_2 = \frac{1}{2}, \dots, N_Z - \frac{1}{2}. \tag{21}$$

Differentiation and integration of (21) with respect to  $R$  and  $Z$  can be performed analytically, as described in Section (III B). In this work we also need differentiation in  $\varphi$ , which can be trivially performed within the trigonometric basis (18).

#### IV. VECTOR POTENTIAL RECONSTRUCTION

In the context of a right-hand side containing a discrete magnetic field  $\mathbf{B}$ , we interpolate  $\mathbf{B}$  indirectly through its vector potential  $\mathbf{A}$ , in order to ensure a divergence-free construction. For this purpose, we first recall that in cylindrical coordinates  $(R, \varphi, Z)$ , the curl of the vector potential  $\mathbf{A}$  gives rise to the magnetic field in component form:

$$B_R = \frac{1}{R} \frac{\partial A_Z}{\partial \varphi} - \frac{\partial A_\varphi}{\partial Z} \quad (22)$$

$$B_\varphi = \frac{\partial A_R}{\partial Z} - \frac{\partial A_Z}{\partial R} \quad (23)$$

$$B_Z = \frac{1}{R} \frac{\partial}{\partial R} (RA_\varphi) - \frac{1}{R} \frac{\partial A_R}{\partial \varphi}. \quad (24)$$

##### A. Rational approximation

In the case of an axisymmetric magnetic field, we have

$$\psi(R, Z) = RA_\varphi \quad (25)$$

$$G(R, Z) = RB_\varphi, \quad (26)$$

where both  $\psi(R, Z)$  and  $G(R, Z)$  are well approximated by polynomials of  $R$  and  $Z$ . Because of this,  $A_\varphi = \psi(R, Z)/R$  and  $B_\varphi = G(R, Z)/R$  are naturally expressed as rational polynomials. This implies that we should not interpolate  $A_\varphi$  and  $B_\varphi$  directly, and instead interpolate the quantities  $RA_\varphi$  and  $RB_\varphi$ . Since the magnetic field's axisymmetric  $B_\varphi$ -component dominates the overall magnetic field in tokamaks, the last statement can also be applied to the full quantities  $RA_\varphi(R, \varphi, Z)$  and  $RB_\varphi(R, \varphi, Z)$ , possibly including non-axisymmetric components. For a general three dimensional toroidal field, both  $\psi(R, \varphi, Z)$  and  $G(R, \varphi, Z)$  will depend on  $\varphi$ ,

$$\psi(R, \varphi, Z) = RA_\varphi(R, \varphi, Z) \quad (27)$$

$$G(R, \varphi, Z) = RB_\varphi(R, \varphi, Z). \quad (28)$$

Given  $\psi$  and  $G$  – which now simply correspond to rescaled versions of  $A_\varphi$  and  $B_\varphi$  rather than the original poloidal and toroidal flux functions in the context of axisymmetric magnetic fields – the relation  $\mathbf{B} = \nabla \times \mathbf{A}$  can be formulated as

$$B_R = \frac{1}{R} \frac{\partial A_Z}{\partial \varphi} - \frac{1}{R} \frac{\partial \psi}{\partial Z} \quad (29)$$

$$G = \frac{\partial RA_R}{\partial Z} - R \frac{\partial A_Z}{\partial R} \quad (30)$$

$$B_Z = \frac{1}{R} \frac{\partial \psi}{\partial R} - \frac{1}{R} \frac{\partial A_R}{\partial \varphi}. \quad (31)$$

Gauge freedom allows us to set one of  $\mathbf{A}$ 's components to vanish, and the form of the  $G$  equation (30) implies a good candidate to be

$$A_Z = 0, \quad (32)$$

together with a new variable

$$\chi(R, \varphi, Z) \equiv RA_R(R, \varphi, Z). \quad (33)$$

From (30), it is easy to see that  $\chi(R, \varphi, Z)$  is well approximated by a polynomial in  $R$  and  $Z$ , because  $G$  is. Finally, the reconstruction of  $\mathbf{A}$ , which is in the form of rational polynomials

$$A_R = \frac{\chi}{R}, \quad A_\varphi = \frac{\psi}{R}, \quad A_Z = 0, \quad (34)$$

is done by integrating

$$-\frac{1}{R} \frac{\partial \psi}{\partial Z} = B_R \quad (35)$$

$$\frac{\partial \chi}{\partial Z} = G = RB_\varphi \quad (36)$$

$$\frac{1}{R} \frac{\partial \psi}{\partial R} - \frac{1}{R^2} \frac{\partial \chi}{\partial \varphi} = B_Z, \quad (37)$$

that is we compute  $\psi$  and  $\chi$  through the magnetic field ( $B_R$ ,  $G=RB_\varphi$ ,  $B_Z$ ) as defined on its given discrete grid. Integrating the first two equations with respect to  $Z$ , we obtain

$$\psi(R, \varphi, Z) = - \int_{Z_0}^Z RB_R(R, \varphi, Z') dZ' + C_1(R, \varphi), \quad (38)$$

$$\chi(R, \varphi, Z) = \int_{Z_0}^Z RB_\varphi(R, \varphi, Z') dZ' + C_2(R, \varphi). \quad (39)$$

Substituting these into the last component equation for  $B_Z$  and using  $\nabla \cdot \mathbf{B} = 0$ , one finds

$$\begin{aligned} \frac{1}{R} \frac{\partial \psi}{\partial R} - \frac{1}{R^2} \frac{\partial \chi}{\partial \varphi} - B_Z &= - \int_{Z_0}^Z \frac{1}{R} \frac{\partial}{\partial R} [RB_R(R, \varphi, Z')] dZ' + \frac{1}{R} \frac{\partial C_1}{\partial R} \\ &\quad - \frac{1}{R} \int_{Z_0}^Z \frac{\partial}{\partial \varphi} B_\varphi(R, \varphi, Z') dZ' - \frac{1}{R^2} \frac{\partial C_2}{\partial \varphi} - B_Z \\ &= \int_{Z_0}^Z \frac{\partial B_Z(R, \varphi, Z')}{\partial Z'} dZ' + \frac{1}{R} \frac{\partial C_1}{\partial R} - \frac{1}{R^2} \frac{\partial C_2}{\partial \varphi} - B_Z \\ &= B_Z(R, \varphi, Z) - B_Z(R, \varphi, Z_0) + \frac{1}{R} \frac{\partial C_1}{\partial R} - \frac{1}{R^2} \frac{\partial C_2}{\partial \varphi} - B_Z(R, \varphi, Z) \\ &= -B_Z(R, \varphi, Z_0) + \frac{1}{R} \frac{\partial C_1}{\partial R} - \frac{1}{R^2} \frac{\partial C_2}{\partial \varphi} \\ &= 0. \end{aligned} \quad (40)$$

This equation can be satisfied by simply taking  $C_2 = 0$  and finding  $C_1$  from

$$C_1(R, \varphi) = \int_{R_0}^R R' B_Z(R', \varphi, Z_0) dR'. \quad (41)$$

Finally, gathering all pieces together, we have

$$\psi(R, \varphi, Z) = - \int_{Z_0}^Z RB_R(R, \varphi, Z') dZ' + \int_{R_0}^R R' B_Z(R', \varphi, Z_0) dR', \quad (42)$$

$$\chi(R, \varphi, Z) = \int_{Z_0}^Z RB_\varphi(R, \varphi, Z') dZ'. \quad (43)$$

## B. Reconstruction procedure

To evaluate (42) and (43), we consider a single poloidal cross-section of a torus representing a tokamak fusion reactor, discretized by a rectangular grid  $\Omega_p = (R_{i_1}, Z_{i_2})$  with points

$$R_{i_1} = R_{\min} + i_1 h_R, \quad (44)$$

$$Z_{i_2} = Z_{\min} + i_2 h_Z, \quad (45)$$

and employ the finite differences (8)-(10) on a finer grid to compute fields and derivatives, with finite difference stencils formed around  $\Omega_p$  grid points. We form Taylor polynomials ( $u^{i_1, i_2}$ ,  $v^{i_1, i_2}$ ,  $w^{i_1, i_2}$ ) on the primal grid  $\Omega_p$ , which approximate the possibly non-divergence free discrete field components,  $B_R$ ,  $B_\varphi$  and  $B_Z$ , respectively. The polynomials are of the form (17). Next, using Section (III C), we obtain interpolation polynomials ( $u^{j_1, j_2}$ ,  $v^{j_1, j_2}$ ,  $w^{j_1, j_2}$ ). This will give a continuous

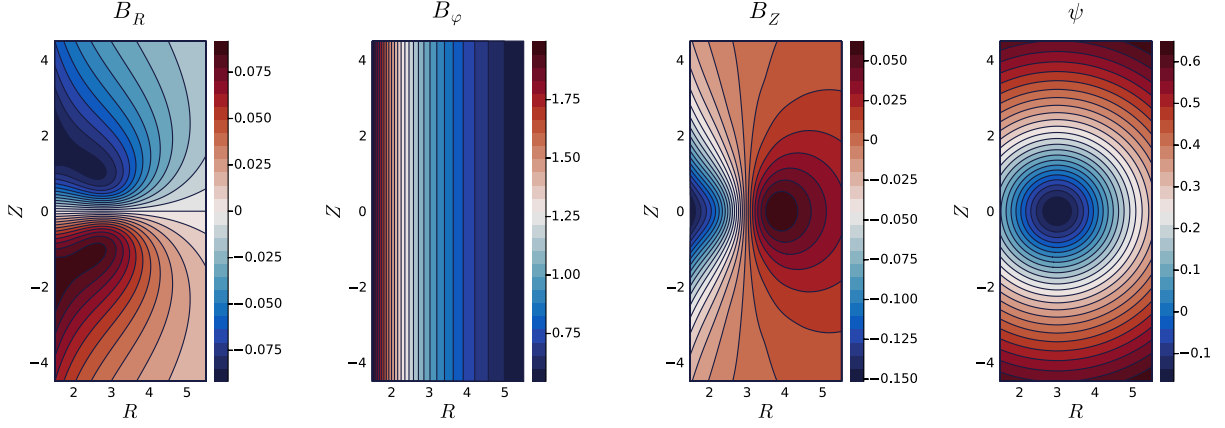


FIG. 2: 9th order Hermite interpolation of analytically constructed magnetic field (54), and reconstructed poloidal flux function on a coarsest mesh. The number of grid points in each direction is given by  $N_R = 5$ ,  $N_Z = 10$ , and the resulting field approximation is continuous, differentiable and divergence free.

representation of the components of  $\mathbf{B}$ , which has  $m_R$  and  $m_Z$  derivatives with guaranteed continuity both locally and across cell interfaces.

The resulting piece-wise polynomial representation can be integrated analytically, see Section (III B), thereby providing a path to compute  $\psi$  and  $\chi$  in (42) and (43). Applying (16) separately in the  $R$  and  $Z$  directions, we obtain

$$\psi(R, \varphi, Z) \approx p^{j_1, j_2}(R, \varphi, Z) = - \int_{Z_c}^Z u(R, \varphi, Z') dZ' + \int_{R_c}^R w(R', \varphi, Z_c) dR', \quad (46)$$

$$\chi(R, \varphi, Z) \approx q^{j_1, j_2}(R, \varphi, Z) = \int_{Z_c}^Z v(R, \varphi, Z') dZ', \quad (R, Z) \in [R_{j_1}^d - \frac{h_R}{2}, R_{j_1}^d + \frac{h_R}{2}] \times [Z_{j_2}^d - \frac{h_Z}{2}, Z_{j_2}^d + \frac{h_Z}{2}], \quad (47)$$

where  $p^{j_1, j_2}$  and  $q^{j_1, j_2}$  are  $(2m_R + 2) \times (2m_Z + 2) \times (N_\varphi + 1)$  and  $(2m_R + 1) \times (2m_Z + 2) \times (N_\varphi + 1)$  piece-wise Taylor-trigonometric polynomials defined locally on each cell.

### C. Field evaluation

Finally, given the approximated vector potential (34) through (46) and (47), we can apply a curl using III B to obtain an interpolated expression for the magnetic field, given by

$$B_R \approx \frac{u(R, \varphi, Z)}{R}, \quad B_\varphi \approx \frac{v(R, \varphi, Z)}{R}, \quad (48)$$

$$B_Z \approx \frac{1}{R} \left( - \int_{Z_c}^Z \frac{\partial u}{\partial R}(R, \varphi, Z') dZ' + w(R, \varphi, Z_c) \right) - \frac{1}{R^2} \int_{Z_c}^Z \frac{\partial v}{\partial \varphi}(R, \varphi, Z') dZ', \quad (49)$$

where

$$u(R, \varphi, Z) = u^{j_1, j_2}(R, \varphi, Z), \quad v(R, \varphi, Z) = v^{j_1, j_2}(R, \varphi, Z), \quad w(R, \varphi, Z) = w^{j_1, j_2}(R, \varphi, Z), \quad (50)$$

$$R_{j_1} - \frac{h_R}{2} < R < R_{j_1} + \frac{h_R}{2}, \quad (51)$$

$$Z_{j_2} - \frac{h_Z}{2} < Z < Z_{j_2} + \frac{h_Z}{2}, \quad (R, Z) \in \Omega_d. \quad (52)$$

Derivatives can be taken by using (13) and trigonometric identities. Since all differentiation is exact, the resulting field's divergence is 0. Moreover if  $m_R > 1$  and  $m_Z > 1$ , its gradient and curl are continuous.

## V. NUMERICAL EXPERIMENTS

### A. Analytical circular flux surfaces: rates of convergence

Consider an axisymmetric magnetic field represented as

$$\mathbf{B} = RB_\phi \nabla \varphi + \nabla \varphi \times \nabla \psi, \quad RB_\phi = \text{const}, \quad (53)$$

where here we set  $RB_\phi$  equal to a constant for simplicity, rather than the usual flux function considered for axisymmetric field configurations. The magnetic field's components are defined with respect to the magnetic axis at  $(R, Z) = (3, 0)$ , where the length has been normalized by a minor radius  $a = 2$  meters, so that the aspect ratio of 3 corresponds to the value of ITER. We then set

$$RB_R(R, Z) = -\frac{Z}{q(R, Z)}, \quad RB_\phi(R, Z) = 3, \quad RB_Z(R, Z) = \frac{R-3}{q(R, Z)}, \quad (54)$$

and for the results presented in this section, the safety factor's profile is given by

$$q(R, Z) = q_0 + q_2(R-3)^2 + q_2 Z^2, \quad q_0 = 2.0, \quad q_2 = 2.1. \quad (55)$$

The poloidal flux function is  $\psi(R, Z) = \frac{\log(q)}{2q_2}$ .

We consider a rectangular domain  $[1, 6] \times [-5, 5]$ , which is discretized with a  $n_R \times n_Z$  regular grid. The number of grid points of the Hermite grid is set to  $N = (n_R - 1)/4$  and  $M = (n_Z - 1)/4$  in the  $R$ - and  $Z$ -directions, respectively. Starting with  $n_R = 21$  and  $n_Z = 41$  grid points in each direction, we measure the error and increase the resolution while keeping the same aspect ratio. For the error measurement, we evaluate an approximation on a finer grid oversampled with 10000 grid points per unit square and compute the  $l_2$  norm of the difference to an exact solution evaluated on the same mesh, relative to the  $l_2$ -norm of the solution. The convergence plot is shown in FIG. (3). Solid lines display the relative errors appearing in the magnetic field component- and poloidal flux function computations, as functions of grid spacing  $h_Z$  in the Hermite interpolation. As indicated by the plot, the  $\psi$  and  $B_R$  approximations converge at fifth order.  $B_Z$  converges at an order decreased by 1. The reason for this decrease is that  $B_Z$  is approximated using a derivative of  $u$  with respect to  $R$ , which truncates at the  $2m_R$  coefficient.

### B. Conservation in guiding center motion

We consider the relativistic guiding center equations<sup>13,23</sup> in the coordinate system  $(p, \xi, \mathbf{X})$ , in the absence of collisions, radiation and the electric field. In terms of dimensionless variables, they can be written as

$$\frac{dp}{dt} = 0, \quad (56)$$

$$\frac{d\xi}{dt} = -\frac{p(1-\xi^2)}{2\gamma \mathbf{B}_\parallel^*} \mathbf{B}^* \cdot \nabla \ln B, \quad (57)$$

$$\frac{d\mathbf{X}}{dt} = \frac{\xi p}{\gamma} \frac{\mathbf{B}^*}{\mathbf{B}_\parallel^*} - \frac{1}{\omega_c} \frac{p^2(1-\xi^2)}{2\gamma \mathbf{B}_\parallel^*} \vec{\mathbf{b}} \times \nabla \ln B, \quad (58)$$

where

$$\gamma = \sqrt{1+p^2}, \quad \mathbf{B}^* = \mathbf{B} - \xi p \nabla \times \vec{\mathbf{b}}, \quad \mathbf{B}_\parallel^* = \mathbf{B}^* \cdot \vec{\mathbf{b}}. \quad (59)$$

Here time  $t$  is normalized by the tokamak's minor radius over the speed of light,  $a/c$ .  $p$  is the particle momentum normalized by  $mc$ ,  $\xi = \frac{p_\parallel}{p}$  is the pitch,  $\mathbf{X}$  is the guiding center position,  $\vec{\mathbf{b}} = \mathbf{B}/B$  is the direction of magnetic field, and  $\omega_c$  is the cyclotron frequency of a charged particle positioned at the magnetic axis.

The purpose of this numerical experiment is to show whether higher smoothness improves the simulation of guiding center motion. The fields are computed by a few steps of a mimetic finite difference method solving the quasistatic magnetohydrodynamic equations in an ITER tokamak domain<sup>24</sup>, and are then interpolated using Hermite interpolation. The interpolated fields are shown in FIG. (5).

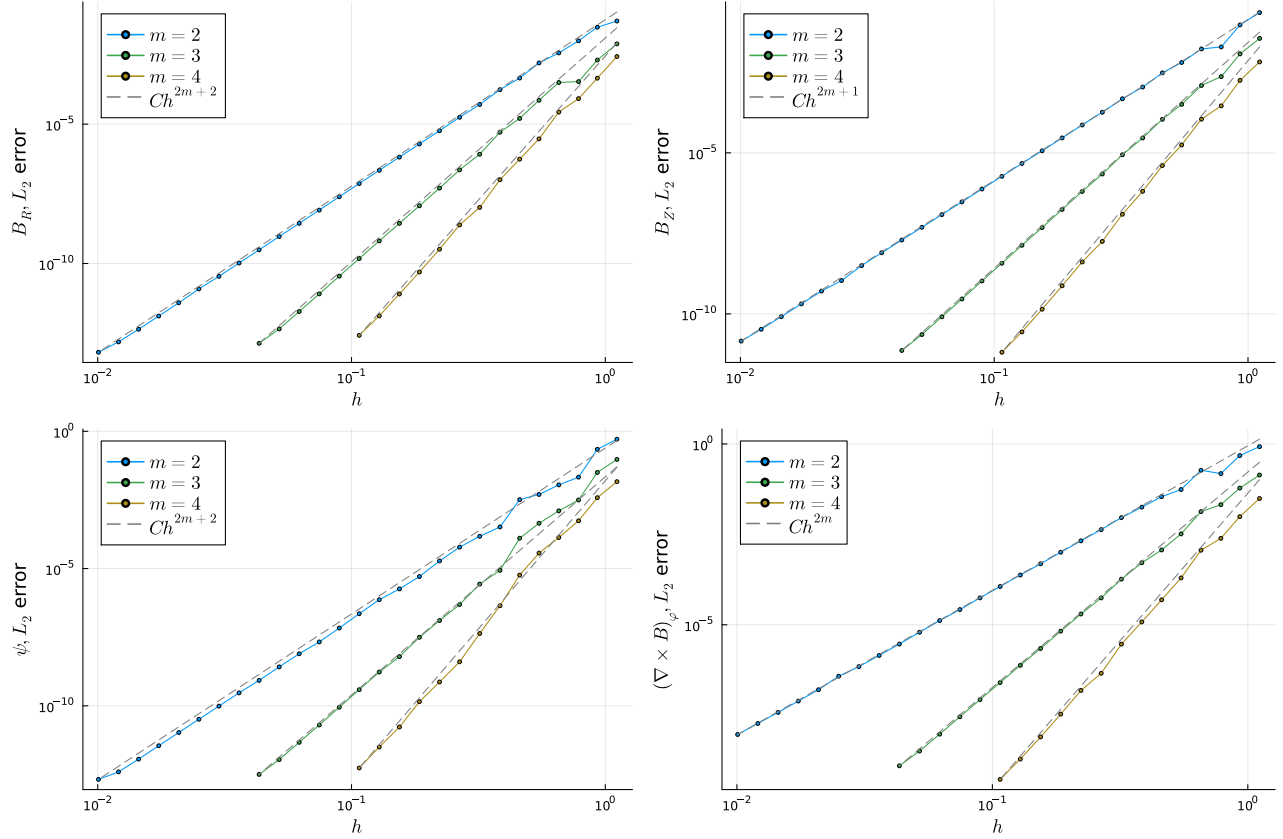


FIG. 3: Hermite interpolation convergence for analytic magnetic fields. Solid lines display the relative error arising when computing magnetic field components and poloidal flux function as a function of grid spacing used in the Hermite interpolation. Dashed lines display the expected convergence rates.  $\psi$  (lower left) and  $B_R$  (upper left) approximations converge at 6th, 8th and 10th order.  $B_\phi$  (not shown) does not have an error because  $RB_\phi$  is a constant and thus is exactly represented in the polynomial basis.  $B_Z$  (upper right) converges at a reduced order (5th, 7th and 9th). The reason for this is that  $B_Z$  is approximated by a derivative of  $u$  with respect to  $R$ , which truncates at the  $2m_R = 4, 6, 8$  coefficients. Further,  $\nabla B$  (lower right) converges at 4, 6 and 8th order.

As a measure of accuracy, we will look at how well the magnetic moment  $\mu$  and toroidal canonical momentum  $p_\phi$  are conserved. In dimensionless variables those become

$$p_\phi = \frac{1}{\omega_c} \xi p b_\phi R - \psi, \quad \mu = \frac{(1 - \xi^2) p^2}{B}. \quad (60)$$

We simulate a randomly distributed particle bunch for half a millisecond, which corresponds to  $10^5 - 10^8$  timesteps, and calculate the discrepancy of  $p_\phi$  and  $\mu$  between the initial time and the final time. The comparison is shown in FIG. (4). In the plot, we display the relative conservation error of  $p_\phi$  and  $\mu$  as a function of the timestep averaged over the particle distribution. The timestep is normalized by the simulation's final time (0.5 ms). This test has been performed with different field interpolation variants, varying  $m$ , i.e. the number of interpolated derivatives. As we can see, the 5th order Runge-Kutta method cannot achieve the theoretical convergence rate in the case of an insufficient smoothness ( $m < 3$ ) for the ITER-type finite difference-based magnetic field, i.e. the numerical solution of the quasistatic equations when the timestep is small. In contrast, for the analytic magnetic field described in the previous section,  $m = 2$  is sufficient. Similar findings hold true for 4th order Runge-Kutta method. The reason for such an inconsistency between numerical and analytic fields is that the interpolation of analytic fields has significantly smaller jumps in high derivatives across the gridlines, although  $m = 2$  only guarantees  $C^2$  continuity of  $\psi$ , ( $C^1$  for the  $B_Z$  component).

Poincaré plots are a practical, effective way of representing complex 3D magnetic fields conveniently. Poincaré plots are generated from the intersection of different magnetic field streamlines with a particular poloidal plane. Provided the streamlines are integrated long enough, it is possible to visualize the shape of the magnetic surfaces. However, the slightest deviation from a divergence-free magnetic field would result in largely perturbed Poincaré plots.

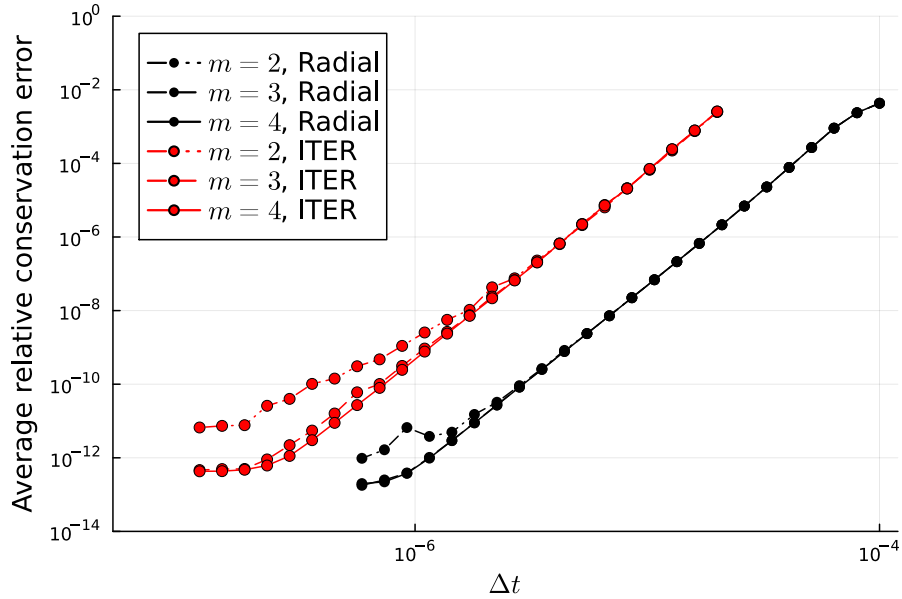


FIG. 4: Guiding center equations conservation-convergence test. Average, relative conservation error of  $p_\phi$  and  $\mu$  as a function of the timestep. The timestep is normalized by 0.5 ms, which is the simulation’s final time. Lines display the conservation errors of the 5th order Runge-Kutta method from the Dormand-Prince embedded pair of solutions. Red lines display the conservation error when background fields are set to the ITER-type VDE simulation, as displayed in FIG. (5). Black lines display the conservation error when background fields are set to analytic fields with radial flux surfaces, as displayed in FIG. (2). Different line styles represent the number of derivatives interpolated using the Hermite method for field reconstruction.

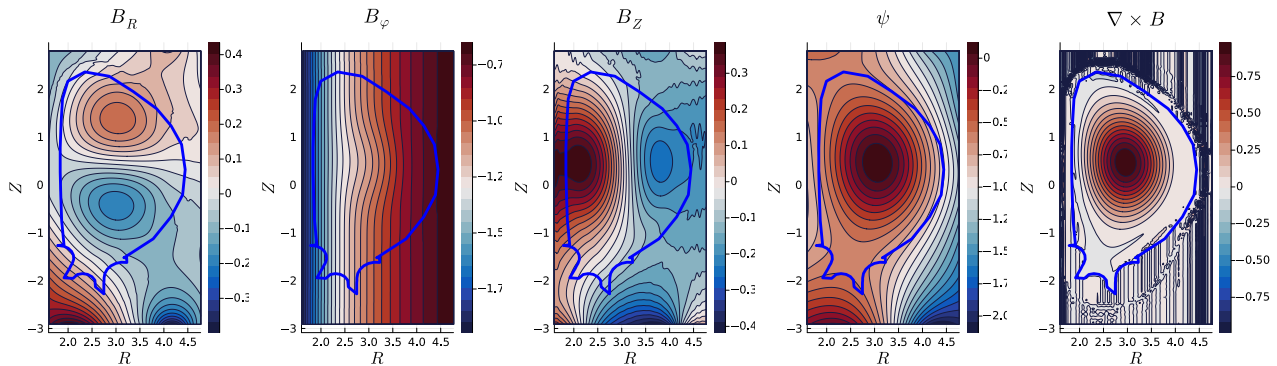


FIG. 5: 9th order accurate Hermite interpolation of ITER magnetic fields, reconstructing the poloidal flux function and toroidal current from a mimetic finite difference discretization. The number of grid points in each direction is  $N_R = 23$ ,  $N_Z = 48$ . The resulting field approximation is continuous, differentiable and divergence free.

In the case of having to analyze fields arising from finite element approximations that are only weakly divergence free, using the proposed methodology below becomes instrumental. Both to recover strictly solenoidal magnetic fields, and to be able to efficiently and accurately integrate the streamlines required to produce Poincaré plots. Moreover, strongly divergence free approximations also benefit from an increased performance when integrating the streamlines.

In order to reconstruct the fields, we evaluate the solution at each node of a Cartesian grid covering the whole finite element domain. For points outside the original domain, the magnetic field is set to be  $\vec{0}$ , which would be a bad solution as the field is evaluated close to the boundary, e.g., for diagnostics beyond the separatrix. In the latter case, it would be beneficial to extend the finite element domain beyond the first wall or to extend the Hermite interpolation beyond the finite element boundary by imposing boundary conditions<sup>17</sup>. Nevertheless, for flux reconstruction it is important to put a point in the center of the domain as the integration bound (i.e. the point  $(R_c, Z_c)$  in (46), (47) and perform the line integration in 4 directions rather than 2 directions from the corner of the domain, so that the error from the outside of the domain

does not propagate inside the domain through integration. Unfortunately such error propagation will inevitably happen in non-convex regions, i.e. below the X-point, around divertor. Then, we use (42)–(43) to find  $\psi$  from the given  $\mathbf{B}$ . Once the flux function is known, we are able to efficiently evaluate the magnetic field and produce the Poincaré plots. To this end, we seek the intersection of the integral curves of  $\mathbf{B}$  with a poloidal plane  $\varphi = \varphi_0$ . That is, we are looking for the solution curves of

$$\frac{d\mathbf{X}}{dt} = \mathbf{B}(\mathbf{X}). \quad (61)$$

In a cylindrical coordinate system, taking  $\varphi$  as an independent variable and applying (48), (49), we obtain

$$\frac{dR}{d\varphi} = \frac{RB_R}{B_\varphi} \approx \frac{Ru}{v}, \quad (62)$$

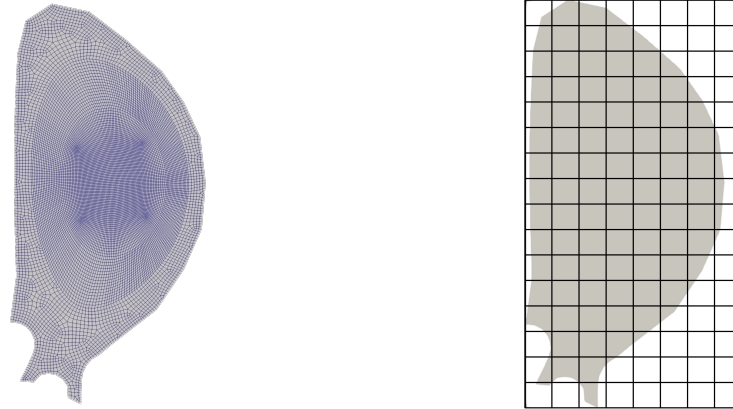
$$\frac{dZ}{d\varphi} = \frac{RB_Z}{B_\varphi} \approx \frac{R}{v} \left( -\int_{Z_c}^Z \frac{\partial u}{\partial R} dZ' + w \Big|_{Z=Z_c} \right) - \frac{1}{v} \int_{Z_c}^Z \frac{\partial v}{\partial \varphi} dZ', \quad (63)$$

which we solve for various initial conditions to the end point  $\varphi = 2\pi k$  for the  $k$ -th toroidal transit to generate the Poincaré plots.

In the next subsections, we show two practical examples for which we have used the methodology described above.

### 1. Linear piecewise continuous fields

Let us consider in this experiment a magnetic field resulting from a first order continuous finite element solution. The solution is obtained using the formulation proposed in a previous work<sup>25</sup>. Using this strategy yields magnetic fields that are not strictly solenoidal, since it is only possible to enforce the projection of  $\nabla \cdot \mathbf{B}$  onto the discrete finite element space to be null.



(a) Original finite element mesh where the field is defined. (b) Cartesian mesh where the solution is interpolated for later analysis. Here each box represents a  $10 \times 10$  mesh block.

FIG. 6: Meshes used to produce Poincaré plots.

We consider a piecewise continuous linear field given on the mesh depicted in FIG. 6a. We evaluate the solution at each node of an 80 by 160 points Cartesian grid covering the domain  $[1.979, 4.3975] \times [-2.205, 2.356]$  (see FIG. 6b). Following the previously described procedure, and integrating equation (63) we are able to efficiently produce Poincaré plots, which are created using four sets of 21 seeds and 100 toroidal transits for each seed. Each set of seeds is spread equally along lines of length  $\{1, 1.8, 1, 2\}$  separated a length 0.2 from the magnetic axis and pitched an angle of  $\{0, 110, 180, 252.5\}$  degrees, respectively. Note that all lengths are non-dimensionalized with respect to the plasma chamber's horizontal radius.

FIG. 7 depicts them for different time steps of a simulation of an ITER major disruption event. Initially, a (1, 1) kink instability is observed, which excites highly disruptive (2, 1) kink mode.

Given the toroidally averaged magnetic field is provided, or for axisymmetric fields, it is also relevant to reconstruct and analyze the poloidal flux function. In FIG 8, we show the flux function for the toroidally averaged field and together with the Poincaré plots.

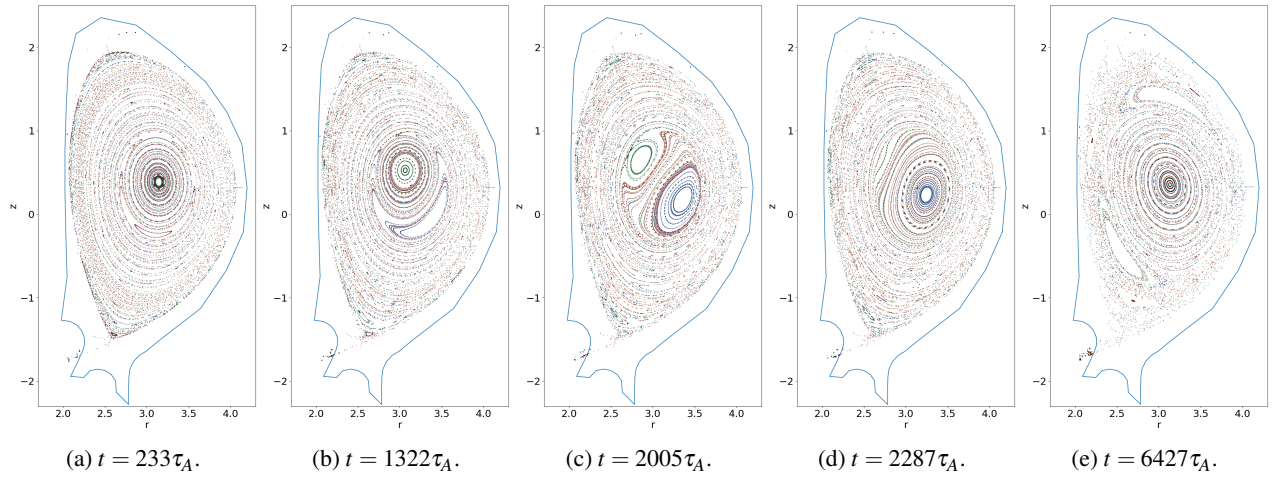


FIG. 7: Poincaré plots at different times using the proposed flux reconstruction of an ITER major disruption event<sup>25</sup>.

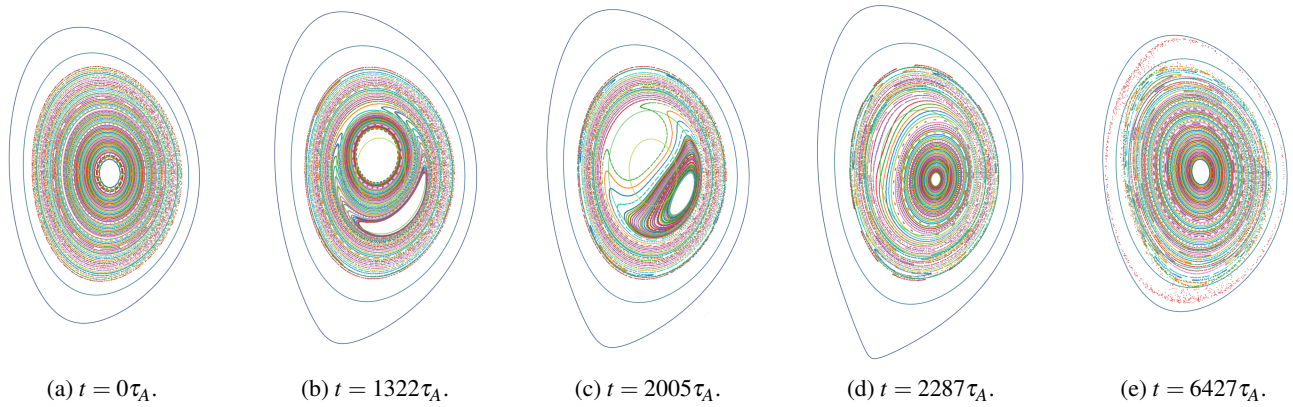


FIG. 8: Flux function for the toroidally averaged field and Poincaré plots at different times.

## 2. Compatible finite element fields

Next, we test our Poincaré plotting routine on compatible finite elements. For this purpose, we first describe our choice of 3D magnetic field configuration as well as mesh and finite element space (see Figure 9). The magnetic field  $\mathbf{B} = \mathbf{B}_0 + k\mathbf{B}_c$  is given by an MHD-equilibrium field  $\mathbf{B}_0$  – which corresponds to a typical setup including nested flux surfaces and one x-point – together with a non-axisymmetric perturbation  $k\mathbf{B}_c$ , for  $k \in \{0, 10, 20, \dots, 80\}$ . The perturbation is given by a magnetic field induced by a current in a “helical” coil embedded inside the reactor chamber. In practice, such coils may be used to break up closed flux surfaces in scenarios such as a vertical displacement event (VDE) after a thermal quench of the plasma. The 3D stochastic magnetic fields thus formed can help deplete the high energy runaway electrons.<sup>26</sup> As in the mimetic difference case, the magnetic field can be discretized in a curl- or div-conforming finite element space in order to preserve (strongly or weakly) the field’s zero weak divergence property. Here, we discretize  $\mathbf{B}$  in the lowest order curl-conforming Nédélec space of the first kind  $Nc_1^c$ . Note that this is unlike the mimetic difference case, which would correspond to the div-conforming Nédélec space of the second kind  $Nc_1^d$ . Finally, the 3D tokamak mesh  $\mathcal{T}_{ext}$  is generated starting from an irregular 2D poloidal plane mesh  $\mathcal{T}_p$ , which is then extruded along the toroidal coordinate  $\varphi$  using 40 poloidal planes. The two layers including the coil’s vertical portion are set to a thickness of  $2\pi/100$  radians; the remaining 38 layers are spread evenly over the remaining  $2\pi(49/50)$  radians.

In order to compute Poincaré plots for the helically perturbed magnetic field  $\mathbf{B} = \mathbf{B}_0 + k\mathbf{B}_p$ , we first need to process the magnetic field’s data. In the case of div- and curl-conforming finite elements, the data is stored as degrees of freedom corresponding to integral moments over facets and edges, respectively. First, we compute the 3D magnetic field’s cylindrical coordinate components  $(\mathbf{B}_r, \mathbf{B}_\varphi, \mathbf{B}_z)$  by projecting  $\mathbf{B}_i \cdot \mathbf{e}_i$  into a 3D second polynomial order scalar discontinuous Galerkin space  $dQ_2(\mathcal{T}_{ext})$ , for unit vectors  $\mathbf{e}_i$  and  $i = r, \varphi, z$ . Note that the choice of space ensures that the degrees of freedom are now associated with coordinates, rather than integral moments. We then compute the first  $l = 5$  Fourier modes in the toroidal di-

rection for each of these three fields. This corresponds to  $1 + 2(l - 1) = 2l - 1$  mode functions in total, given by the constant mode together with the sine and cosine field for each of the  $(l - 1)$  higher modes. In practice, since our mesh is constructed as an extrusion in the  $\varphi$ -direction, this can be done using appropriate summations along  $\varphi$  for degrees of freedom sharing the same  $(r, z)$ -coordinates. Having integrated over  $\varphi$ , these  $3 \times (2l - 1)$  Fourier fields are then functions in the 2D scalar discontinuous Galerkin space  $dQ_2(\mathcal{T}_p)$ . Finally, we interpolate the 2D Fourier fields into the space  $dQ_2(\mathcal{T}_{reg})$ , where  $\mathcal{T}_{reg}$  is a regular rectangular 2D mesh corresponding to a  $N_r \times N_z = 40 \times 80$  grid, and whose underlying rectangular domain contains the toroidal cross-section domain on which  $\mathcal{T}_p$  is defined. At this point, the fields in  $dQ_2(\mathcal{T}_{reg})$  then have degree of freedom values associated with the  $l$  Fourier modes' values at a regularly spaced set of coordinates, as required for our Poincaré plotting routine. Note that overall, this means that the original data for  $\mathbf{B}_0$  is first interpolated from the regular fine MHD equilibrium code grid onto the semi-irregular coarse finite element mesh  $\mathcal{T}_{ext}$ , and then interpolated back to a coarse regular grid. One may therefore expect a significant interpolation error that may interfere with the Poincaré plotting routine's performance.

The Poincaré plots are created using 31 seeds and 1000 toroidal transits for each seed. The seeds are spread equally along a line of length 2.4 (noting that the domain is non-dimensionalized with respect to the plasma chamber's horizontal radius), containing the magnetic axis of  $\mathbf{B}_0 + k\mathbf{B}_c$ , pitched at an angle of  $\pi/4$  radians. The resulting plots are shown in FIG. 10.

The case  $k = 0$  corresponds to the equilibrium field  $\mathbf{B}_0$  only, and we find that the Poincaré plotting routine recovers the closed flux surface structure very well, in spite of the aforementioned interpolation error. As  $k$  increases, we find that as expected, the perturbing magnetic field arising from an asymmetric coil current increasingly breaks up the surfaces, leading to an increasingly stochastic magnetic field profile. Altogether, this demonstrates that our Poincaré plotting routine effectively reproduces the expected magnetic field behavior for lowest order compatible spaces defined on coarse, semi-regular finite element meshes.

## VI. SUMMARY

We presented a method for reconstructing divergence-free continuous magnetic fields via vector potentials, with a choice of high order continuity based on Hermite interpolation. It is designed for applications when high order adaptive ODE solvers are used to push particles or integrate the field lines for Poincaré section analysis, especially if the optimal integration order and a timestep adjustment is desired. If the input field data is exact, the guaranteed  $C(m)$  continuity comes with a  $(2m) - (2m + 2)$  order of accuracy of field components and poloidal flux function approximation. This was demonstrated in section V A.

Further, the volume preserving and high order continuity properties of Hermite interpolation with vector potential reconstruction were tested on the relativistic Guiding Center Equations. Here, it is crucial to guarantee conservation of toroidal canonical momentum and magnetic moment, at least to a small tolerance for accuracy of long term simulations. In section V B, it has been shown that insufficient derivative continuity of the discrete background magnetic field does degrade the order of Runge-Kutta schemes, especially at low error tolerances. We studied this behavior in section II, and our findings can be summarized as follows. Consider a simple ODE  $y' = f(y)$  and local truncation error of a 4th order Runge-Kutta method, in the vicinity of a 3rd derivative discontinuity

$$\varepsilon \sim C\Delta t^5 + \alpha(f_+^{(3)} - f_-^{(3)})\Delta t^4, \quad (64)$$

where  $\alpha$  and  $C$  are constants that depend on  $f$ , and the  $+/-$  notation indicates the right and left 3rd derivative of the right-hand side function. In the perfectly smooth case, the second term would cancel out and the local truncation error becomes  $O(\Delta t^5)$ . Additionally, the method will also achieve a near optimal order of convergence in the discontinuous case, for high error tolerances when the first term dominates and the jump  $(f_+^{(3)} - f_-^{(3)})$  is small.

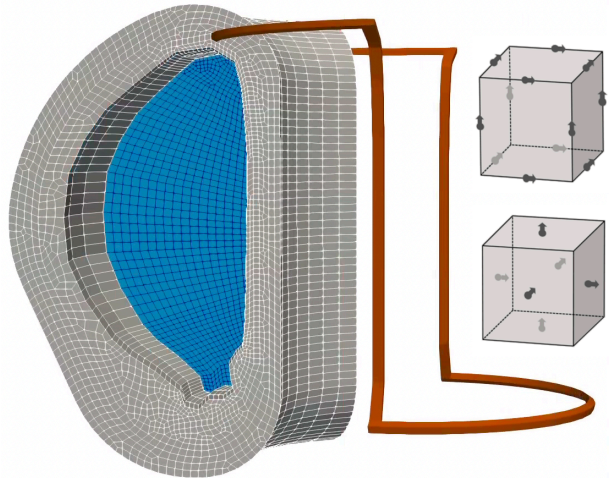


FIG. 9: Mesh and space setup for finite-element based Poincaré plots. Left: Mesh cutout including plasma (blue), wall (grey), and coil (brown) regions. Right: curl- (top) and div- (bottom) conforming hexahedral finite elements for the spaces  $Nc_1^e$  and  $Nc_1^f$ , respectively, with degrees of freedom in marked dark grey.

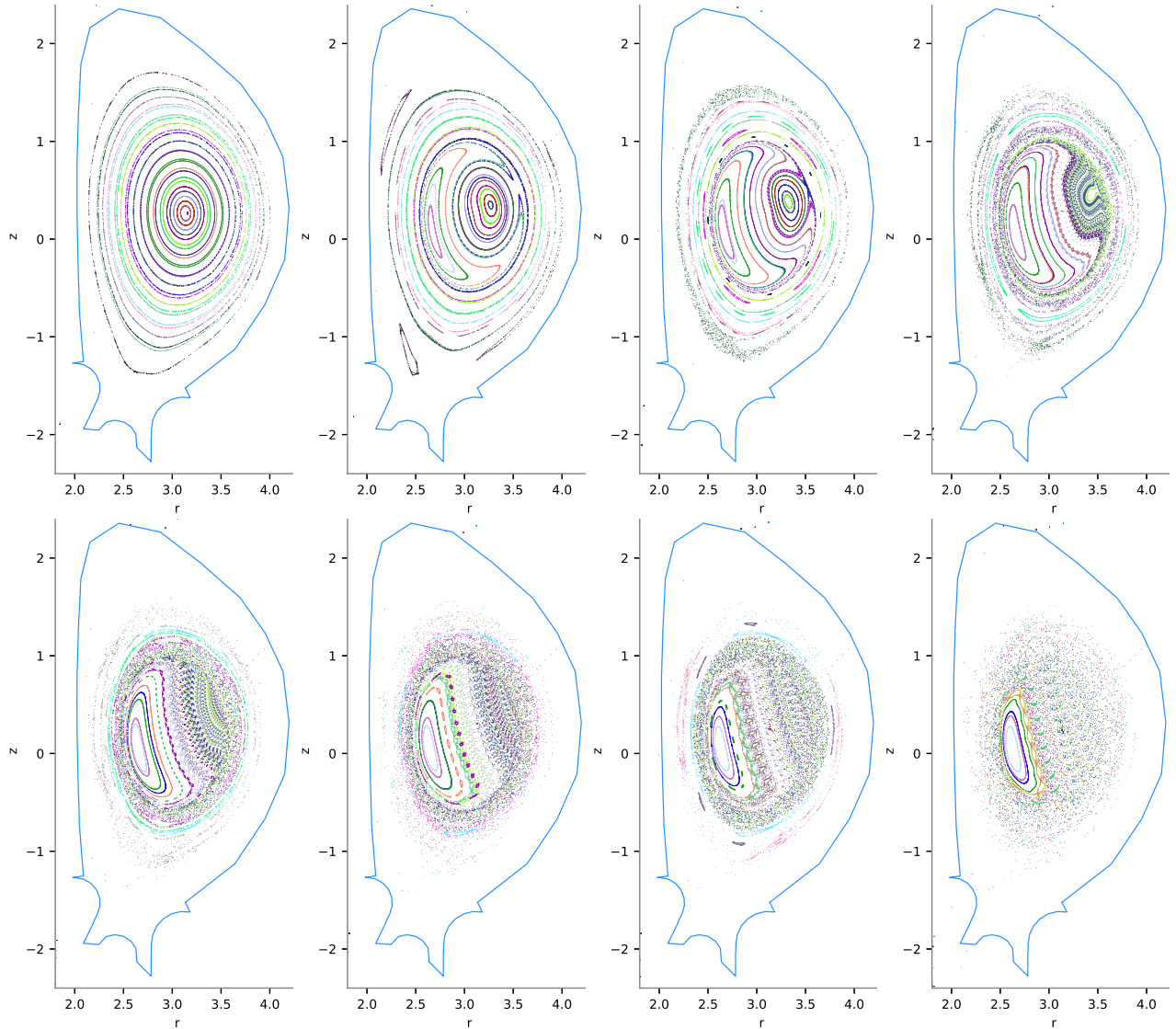


FIG. 10: Poincaré plots for equilibrium magnetic field perturbed by a helical coil, for perturbation strengths  $k \in \{0, 10, 20, \dots, 80\}$  (left to right, top to bottom). Following a non-dimensionalization, the  $R$  and  $Z$  coordinates are scaled by  $L_0 = 1/2$ .

Alternatively, Runge-Kutta methods can be used for discontinuous right-hand sides preserving the optimal order of convergence using dense output techniques (also based on Hermite interpolation) as described in<sup>19</sup>. However, in many particle applications this may become inefficient, as it requires employing root-finding mechanisms for each particle individually each time it crosses an interface. Nevertheless, this would be an interesting method to test in future work.

## VII. ACKNOWLEDGEMENT

We thank the U.S. Department of Energy (DOE) Office of Fusion Energy Sciences and Office of Advanced Scientific Computing Research for support under the Tokamak Disruption Simulation SciDAC project and the magnetic fusion theory program, at the Los Alamos National Laboratory (LANL) under DOE Contract No. 89233218CNA000001. Additional support to Beznosov and Tang was provided by the LANL LDRD Program under Exploratory Research project 20250556ER. This research used resources provided by the Los Alamos National Laboratory Institutional Computing Program, which is supported by the U.S. Department of Energy's National Nuclear Security Administration under Contract No. 89233218CNA000001, and the National Energy Research Scientific Computing Center (NERSC), a U.S. Department

of Energy Office of Science User Facility located at Lawrence Berkeley National Laboratory, operated under Contract No. DE-AC02-05CH11231 using NERSC award FES-ERCAP0028152.

- <sup>1</sup>M. Zhang and X. Feng, “A comparative study of divergence cleaning methods of magnetic field in the solar coronal numerical simulation,” *Frontiers in Astronomy and Space Sciences* **3** (2016), 10.3389/fspas.2016.00006.
- <sup>2</sup>G. Tóth, “The  $\nabla \cdot b = 0$  constraint in shock-capturing magnetohydrodynamics codes,” *Journal of Computational Physics* **161**, 605–652 (2000).
- <sup>3</sup>A. Dedner, F. Kemm, D. Kröner, C.-D. Munz, T. Schnitzer, and M. Wessberg, “Hyperbolic divergence cleaning for the mhd equations,” *Journal of Computational Physics* **175**, 645–673 (2002).
- <sup>4</sup>K. Lipnikov, G. Manzini, and M. Shashkov, “Mimetic finite difference method,” *Journal of Computational Physics* **257**, 1163–1227 (2014), physics-compatible numerical methods.
- <sup>5</sup>K. Lipnikov, J. Moulton, and D. Svyatskiy, “A multilevel multiscale mimetic (m3) method for two-phase flows in porous media,” *Journal of Computational Physics* **227**, 6727–6753 (2008).
- <sup>6</sup>L. Beirão da Veiga, V. Gyrya, K. Lipnikov, and G. Manzini, “Mimetic finite difference method for the stokes problem on polygonal meshes,” *Journal of Computational Physics* **228**, 7215–7232 (2009).
- <sup>7</sup>L. Beirão Da Veiga, “A mimetic discretization method for linear elasticity,” *ESAIM: Mathematical Modelling and Numerical Analysis* **44**, 231–250 (2010).
- <sup>8</sup>B. da Veiga, J. Droniou, and G. Manzini, “A unified approach for handling convection terms in finite volumes and mimetic discretization methods for elliptic problems,” *IMA Journal of Numerical Analysis* **31**, 1357–1401 (2010), <https://academic.oup.com/imajna/article-pdf/31/4/1357/1952642/drq018.pdf>.
- <sup>9</sup>A. Cangiani, G. Manzini, and A. Russo, “Convergence analysis of the mimetic finite difference method for elliptic problems,” *SIAM Journal on Numerical Analysis* **47**, 2612–2637 (2009).
- <sup>10</sup>F. Brezzi, K. Lipnikov, M. Shashkov, and V. Simoncini, “A new discretization methodology for diffusion problems on generalized polyhedral meshes,” *Computer Methods in Applied Mechanics and Engineering* **196**, 3682–3692 (2007), special Issue Honoring the 80th Birthday of Professor Ivo Babuska.
- <sup>11</sup>K. Yee, “Numerical solution of initial boundary value problems involving maxwell’s equations in isotropic media,” *IEEE Transactions on Antennas and Propagation* **14**, 302–307 (1966).
- <sup>12</sup>J. M. Finn and L. Chacón, “Volume preserving integrators for solenoidal fields on a grid,” *Physics of Plasmas* **12** (2005).
- <sup>13</sup>C. J. McDewitt, Z. Guo, and X.-Z. Tang, “Avalanche mechanism for runaway electron amplification in a tokamak plasma,” *Plasma Physics and Controlled Fusion* **61**, 054008 (2019).
- <sup>14</sup>C. J. McDewitt and X.-Z. Tang, “Runaway electron current reconstitution after a nonaxisymmetric magnetohydrodynamic flush,” *Phys. Rev. E* **108**, L043201 (2023).
- <sup>15</sup>J. Goodrich, T. Hagstrom, and J. Lorenz, “Hermite methods for hyperbolic initial-boundary value problems,” *Mathematics of computation* **75**, 595–630 (2006).
- <sup>16</sup>D. Appelö, T. Hagstrom, and A. Vargas, “Hermite methods for the scalar wave equation,” *SIAM Journal on Scientific Computing* **40**, A3902–A3927 (2018), <https://doi.org/10.1137/18M1171072>.
- <sup>17</sup>O. Beznosov and D. Appelö, “Hermite-discontinuous galerkin overset grid methods for the scalar wave equation,” *Communications on Applied Mathematics and Computation* **3**, 391–418 (2021).
- <sup>18</sup>F. Lekien and J. Marsden, “Tricubic interpolation in three dimensions,” *International Journal for Numerical Methods in Engineering* **63**, 455–471 (2005).
- <sup>19</sup>E. Hairer, G. Wanner, and S. P. Nørsett, *Solving Ordinary Differential Equations I: Nonstiff Problems*, 2nd ed. (Springer, 1993).
- <sup>20</sup>J. R. Dormand and P. J. Prince, “A family of embedded runge-kutta formulae,” *Journal of computational and applied mathematics* **6**, 19–26 (1980).
- <sup>21</sup>B. Fornberg, “Generation of finite difference formulas on arbitrarily spaced grids,” *Mathematics of computation* **51**, 699–706 (1988).
- <sup>22</sup>T. Hagstrom and D. Appelö, “Solving pdes with hermite interpolation,” (Springer, 2015) pp. 31–49.
- <sup>23</sup>J. R. Cary and A. J. Brizard, “Hamiltonian theory of guiding-center motion,” *Reviews of modern physics* **81**, 693–738 (2009).
- <sup>24</sup>Z. Jortí, Q. Tang, K. Lipnikov, and X.-Z. Tang, “A mimetic finite difference based quasi-static magnetohydrodynamic solver for force-free plasmas in tokamak disruptions,” *arXiv preprint arXiv:2303.08337* (2023).
- <sup>25</sup>J. Bonilla, J. N. Shadid, X.-Z. Tang, M. M. Crockatt, P. Ohm, E. G. Phillips, R. P. Pawlowski, S. Conde, and O. Beznosov, “On a fully-implicit vms-stabilized fe formulation for low mach number compressible resistive mhd with application to mcf,” *Computer Methods in Applied Mechanics and Engineering* **417, Part B** (2023), 10.1016/j.cma.2023.116359.
- <sup>26</sup>H. M. Smith, A. H. Boozer, and P. Helander, “Passive runaway electron suppression in tokamak disruptions,” *Physics of Plasmas* **20**, 072505 (2013), [\\_eprint: https://pubs.aip.org/aip/pop/article-pdf/doi/10.1063/1.4813255/16030770/072505\\_1\\_online.pdf](https://pubs.aip.org/aip/pop/article-pdf/doi/10.1063/1.4813255/16030770/072505_1_online.pdf).